IEEE Access
Multidisciplinary ⋮ Rapid Review ⋮ Open Access Journal

Received 18 September 2026, accepted 6 October 2026, date of publication 9 October 2026, date of current version 16 October 2026.

Digital Object Identifier 10.1109/ACCESS.2026.3742223

RESEARCH ARTICLE

Mitigating Non-Target Reflections in GNSS-IR Using a Low-Cost Directional Antenna

UTKAN MUSTAFA DURDAĞ[1], ÖMER KASAR[2], CEMALI ALTUNTAS[3], HAYRUNNISA UMUTLU[2], AND SIMON WILLIAMS[4]

[1]Department of Geomatic Engineering, Artvin Çoruh University, 08010 Artvin, Türkiye
[2]Department of Electronics and Communication Engineering, Karadeniz Technical University, 61080 Trabzon, Türkiye
[3]Department of Geomatic Engineering, Yıldız Technical University, 34220 Istanbul, Türkiye
[4]National Oceanography Centre, L3 5DA Liverpool, U.K.

Corresponding author: Ömer Kasar (omerkasar@ktu.edu.tr)

This work was supported in part by the Karadeniz Technical University Scientific Research Projects Coordination Unit under Grant FBA-2026-11233, and in part by the Artvin Çoruh University Scientific Research Projects Coordination Unit under Grant 2021.F40.02.01.

ABSTRACT Global Navigation Satellite Systems Interferometric Reflectometry (GNSS-IR) retrieves environmental variables from the interference between direct and surface reflected signals. Unwanted contributions are commonly removed by azimuth masking, which acts on the computed satellite azimuth rather than on the direction of arrival, so reflections from outside the selected sector remain in the recorded signal-to-noise ratio data and cannot be separated afterwards. Data from HNLC, a coastal GNSS station next to a strongly reflecting roof, illustrate this limitation. The novelty is hardware restriction of the angular response, at the aperture and before recording. A low-cost 3D-printed Dual Ridged Horn Antenna (DRHA) concentrates sensitivity in the sector of the target surface and suppresses arrivals from behind. It was deployed at a fixed reflecting surface with a low-cost receiver and compared against a commercial patch antenna in its conventional zenith-up orientation on the same receiver, under the same azimuth mask, with single-frequency observations from three constellations. The DRHA returned a median of 2.991 m against an in-situ reflector height of 2.99 m, with a median absolute deviation of 0.226 m consistent across GPS, GLONASS and BeiDou, while the patch median was displaced by 1.538 m from its own in-situ height, with a five times larger deviation. Median peak-to-background noise ratios were 4.89 against 3.73 overall and 4.59 against 3.78 over 16 matched GPS pairs (Wilcoxon signed-rank, $p = 0.056$). As a proof of concept, hardware-level angular selectivity is a practical, low-cost complement to masking where the target cannot be isolated in the data domain.

INDEX TERMS GNSS-IR, signal-to-noise ratio, reflectometry, sea level, directional antenna.

I. INTRODUCTION

Global Navigation Satellite Systems Interferometric Reflectometry (GNSS-IR) exploits the interference between direct and surface reflected signals to sense environmental variables such as sea level, soil moisture, snow depth, and vegetation height [1], [2], [3], [4], [5], [6], [7], [8], [9], [10]. The method operates on Signal-to-Noise Ratio (SNR) observations, in which the oscillation frequency encodes the geometric path difference between the direct and the reflected signal at the receiving antenna [2], [4]. Reflector height retrievals at the centimeter level have been reported over water, snow, and agricultural surfaces [2], [3], [4], [5], [6], and the increasing availability of open data, processing toolboxes, and affordable receiver modules has widened the range of groups able to apply the technique [7], [8], [9], [10], [11], [12], [13]. Several open-source implementations are now available, including MATLAB and Python packages for SNR-based retrieval [7], [8], [11], [12], [39]. The set of variables accessible to SNR based sensing continues to grow, and recent work has examined how SNR amplitude responds to rainfall events over different surface types [30].

Low-cost hardware has been central to this development. Commercial receiver modules combined with simple

The associate editor coordinating the review of this manuscript and approving it for publication was Andrea Tani.

© 2026 The Authors. This work is licensed under a Creative Commons Attribution 4.0 License.
For more information, see https://creativecommons.org/licenses/by/4.0/

antennas have been used for water level, snow, and soil moisture monitoring [9], [24], [25], [26], [27]. In most of these systems the receiving element is a patch or omnidirectional antenna designed for positioning, where the reflected component is an error source to be minimized. GNSS-IR inverts that premise, since the reflected component carries the information, and the instrumentation is therefore used outside the conditions it was designed for.

Because such an antenna accepts energy over a wide angular range, unwanted contributions are usually handled after acquisition through elevation and azimuth masks [19]. This practice is effective in many settings, but it operates in the data domain. A mask is applied to the computed azimuth of the satellite, which follows from the receiver position and the broadcast orbit. It selects which satellite arcs are retained. It does not select which reflections were recorded. At a given epoch the SNR value is the coherent sum of the direct signal and of the reflected and scattered components reaching the antenna from all directions, so a contribution from a structure behind the receiver is present in arcs whose computed azimuth lies inside the retained sector. At open sites the consequence is minor. At sites where a strong reflector stands close to the antenna, no post processing step can recover the target response once the two contributions have been summed at the antenna.

Antenna configuration has already been used to shape which reflections a GNSS-IR installation records. Geodetic antennas are designed for a gain pattern that peaks near the zenith and decreases towards the horizon, which suits positioning but attenuates the low elevation arcs that carry reflectometric information [6], [14], [15]. Side-looking installations address this by reorienting the antenna. Santamaría-Gómez and Watson placed an antenna sideways, with the ground plane vertical and directed in azimuth towards the sea surface, to strengthen the SNR interference near the horizon, and used the resulting data for remote leveling of a tide gauge [28]. A comparison of zenith looking and horizon looking configurations at the same site showed that the horizon looking arrangement recovers reflector heights from elevation ranges in which the zenith looking arrangement receives reflected signals weakly [29]. These studies establish antenna gain distribution as an effective means of control in GNSS-IR. What they modify is the elevation domain, since reorienting an antenna redistributes gain with respect to elevation angle while the response remains close to uniform in azimuth.

The present work applies a similar principle in the azimuth domain. A dual ridged horn antenna (DRHA) is used to concentrate sensitivity in a chosen azimuth sector and to attenuate contributions arriving from behind the antenna, so that angular filtering acts at the aperture, before recording. The antenna is produced by fused deposition modeling with a metal coated surface, an approach that has replaced machined metal in a growing number of microwave components and keeps the cost and weight of the resulting system low [20], [21], [22], [23].

The contribution is threefold. First, the limitation of azimuth masking is demonstrated with data from a coastal GNSS station located next to a strongly reflecting structure. Second, a low-cost directional antenna intended for this situation is described. Third, the antenna is deployed with a low-cost receiver alongside a commercial patch antenna in its conventional zenith-up orientation, and the recorded data are examined through the azimuthal distribution of spectral peak strength and through reflector height retrievals, using single frequency observations from three satellite constellations. The experiment is a proof of concept. It addresses whether the intended angular behavior is present in a real installation, and it is not a long-term performance assessment.

The remainder of the paper is organized as follows. Section II examines angular filtering in GNSS-IR and presents the coastal station. Section III describes the antenna. Section IV covers the field experiment and the processing chain. Section V presents the results, and Section VI discusses them and concludes.

II. ANGULAR FILTERING IN GNSS-IR

Unwanted reflections in GNSS-IR are conventionally handled after acquisition, by restricting the analysis to satellite arcs whose elevation and azimuth fall within a selected range. These masks are computed from the receiver position and the satellite orbits, and are applied to the recorded data. The approach is established practice and works at most sites, but it rests on an assumption about where the recorded signals originate. This section examines that assumption, describes what a geometry-based mask leaves behind, and presents a coastal GNSS station at which the residual effect is apparent.

A. DATA DOMAIN MASKING AND ITS LIMITS

The GNSS-IR forward model describes the detrended SNR (dSNR) as an interference term between the direct and the reflected signal. For a single planar horizontal surface located a vertical distance h below the antenna phase center, the dSNR varies with the satellite elevation angle E as in

$$dSNR\,(E) = A\cos\left(\frac{4\pi h}{\lambda}\sin E + \varphi\right) \tag{1}$$

where λ is the carrier wavelength, A is the amplitude of the interference term and φ is a phase offset [5], [15]. Expressed with respect to the variable $\sin E$, the term is a sinusoid of frequency

$$f = \frac{2h}{\lambda} \tag{2}$$

so that a spectral estimate of f gives the reflector height through $h = \lambda f/2$. This relation underlies most GNSS-IR retrievals [4], [7].

Equation (1) assumes that one surface contributes. At a real site the antenna receives the direct signal together with reflected and scattered components from every surface within its angular coverage, and the dSNR is the sum of the

corresponding interference terms,

$$dSNR\,(E) = \sum_{k=1}^{K} A_k \cos\left(\frac{4\pi h_k}{\lambda}\sin E + \varphi_k\right) \quad (3)$$

where h_k is the apparent reflector height associated with contribution k. The amplitude of each term depends on the reflection coefficient of the surface, on its roughness and extent, and on the response of the receiving antenna in the direction from which that contribution arrives,

$$A_k \propto \Gamma_k G\,(\theta_k, \alpha_k) \quad (4)$$

where Γ_k is the effective reflection coefficient of the surface, G is the antenna gain pattern, and θ_k and α_k are the elevation and azimuth of the arrival direction [13], [38]. The summation in Equation (3) takes place at the antenna. What the receiver records at each epoch is a single scalar in which the individual terms are no longer separable.

An elevation and azimuth mask is defined in terms of the satellite direction. For each epoch the receiver position and the satellite orbit give the elevation E and the azimuth α_s of the transmitting satellite, and the mask retains the arcs for which α_s falls inside a selected sector. The choice of sector is guided by the specular point geometry of the target surface. For a horizontal surface at height h the specular reflection point lies in the vertical plane containing the satellite direction, at a horizontal distance

$$d = \frac{h}{\tan E} \quad (5)$$

from the antenna, so the sector is chosen to place the specular points of the retained arcs on the surface of interest [7], [19].

The mask therefore operates on the index set of the recorded data. It is an indicator function that retains or discards complete arcs, and within a retained arc it multiplies every term of Equation (3) by the same factor. The antenna response operates on the coefficients of the sum, since it scales each A_k according to the direction of arrival before the summation takes place. The two act on different quantities. A mask can discard an arc whose satellite azimuth points away from the target surface, but it cannot alter the contribution of a reflector located outside the retained sector to an arc that has been kept. The condition that α_s falls inside the sector constrains the direction of the transmitter, not the direction from which the reflected components arrive.

It might appear that the terms of Equation (3) can be separated after acquisition, since contributions with distinct apparent heights occupy distinct positions in a spectral estimate. This holds only under restrictive conditions. The height resolution of a spectral estimate computed over an arc is limited by the span of sin E covered by that arc,

$$\Delta h = \frac{\lambda}{2\Delta\,(\sin E)} \quad (6)$$

and arcs used in GNSS-IR are restricted to a chosen elevation band, so that contributions with sufficiently similar apparent heights fall within the same spectral feature and are not resolved [7]. Sampling the spectrum on a finer height grid does not change this. The limit concerns the separation of two contributions and not the estimation of a single one, since the position of an isolated dominant peak can be determined to a small fraction of Δh when the peak stands well above the background. More importantly, Equation (3) presumes that every contribution behaves as a sinusoid in sin E, which is the case for a horizontal planar surface. A vertical facade, a sloping roof or an irregular structure produces a path difference whose variation with elevation angle does not follow the same form, so the associated contribution is not confined to a single spectral peak. Its power is distributed across the spectrum, where it raises the background level against which the target peak is detected. The consequence is a reduction of the peak-to-background noise ratio, not the appearance of a clearly identifiable spurious peak, and no choice made in post processing recovers the target response from data in which this has already occurred.

Whether this matters at a given site depends on the strength of the non-target contributions relative to the target contribution. A surface that is distant, rough or weakly reflecting produces terms with small A_k, and the retrieval is unaffected in practice. This is the situation at most GNSS-IR installations, and it explains why masking has been sufficient in the majority of reported applications. The situation changes when a large, smooth and strongly reflecting structure stands close to the antenna. Such a structure subtends a wide solid angle at the antenna, its reflection coefficient is high, and the corresponding A_k becomes comparable with that of the target surface. Because a conventional GNSS antenna has a gain pattern that is close to uniform in azimuth, no attenuation is applied to these contributions at the point of reception.

This identifies the property required of the receiving element. What is needed is not a narrower mask but an angular response that distinguishes the azimuth sector containing the target surface from the sector containing the non-target reflector, while retaining sufficient gain at the low elevation angles that carry the reflectometric information. An antenna with this property applies the angular restriction to the incoming field, so that the terms of Equation (3) associated with the non-target reflector are attenuated before the summation and before the data are recorded.

B. A COASTAL STATION WITH A NON-TARGET REFLECTOR

The station HNLC records GNSS observations at the end of a pier in Honolulu, Hawaii, with a Trimble NetR9 receiver and an ASH700936D_M antenna. The site is co-located with a NOAA tide gauge (Honolulu, station 1612340), which is not needed for the present example since the approximate antenna height above the water is known. The antenna stands approximately 5.6 m above the water, and the retrievals use arcs between 3 and 15 degrees in elevation over an azimuth sector directed across the water, so that the specular points fall on the sea surface. Figure 1 (top) shows the site. Across the water to the south of the antenna stands a warehouse with a large sloping metal roof, at a distance of roughly 50 m. The

mask is appropriate for the target surface, and the difficulty at this site is not a poorly chosen sector.

The roof geometry determines where its reflections enter the recorded data. Surface heights from a lidar survey define the roof as a sloping planar section, and first order specular geometry applied to this surface gives, for each point on it, the satellite direction from which a signal reflects into the antenna. Figure 1 (bottom) marks the directions that fall inside the elevation and azimuth range used at the station. The affected region spans azimuths of roughly 180 to 220 degrees and elevation angles from about 3 to 15 degrees, with the interference expected at higher elevation angles as the azimuth decreases. Every arc crossing this region satisfies the mask, since the satellite stands over the water, and every such arc records the roof reflection together with the water reflection.

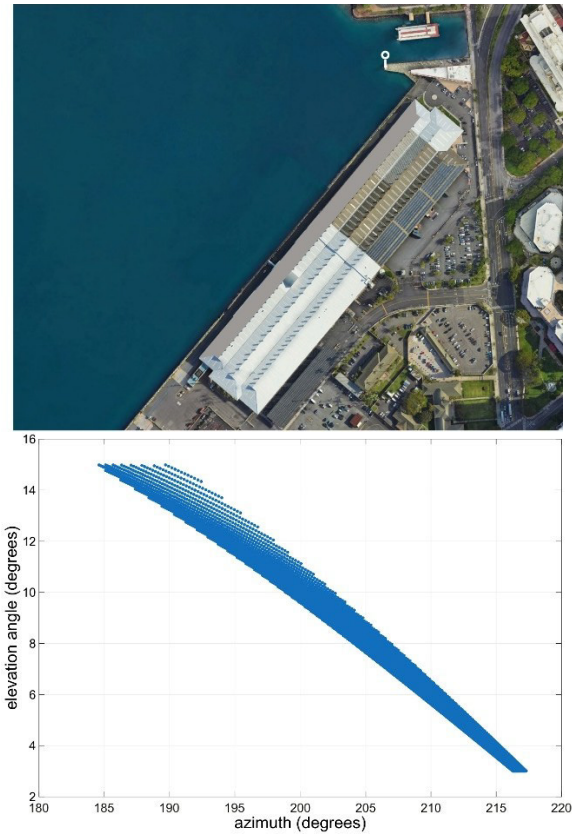


FIGURE 1. The HNLC station and the expected footprint of the roof reflection. (Top) Aerial view of the site, with the antenna position marked at the end of the pier and the warehouse roof to its south across the water. Imagery from Google Earth, Data USGS, Image ©2026 Airbus. (Bottom) Satellite directions from which a signal reflects off the roof into the antenna, computed with first order specular geometry from a lidar derived model of the roof surface and restricted to the elevation and azimuth range used in the sea level processing at the station.

Figure 2 shows the dSNR and its wavelet transform for an arc of GPS PRN 30 on L1, at an azimuth near 205.6 degrees, inside the region identified in Figure 1. Two contributions are present in the same data. A component near the expected water level appears across the arc, and a stronger component between about 8 and 13 degrees in elevation drifts upward in apparent height, the behavior expected of a sloping reflector for which the path difference does not follow Equation (1). The interference occupies the elevation range predicted by the geometry, extending somewhat beyond it, as expected once the finite extent of the reflecting zone around each specular point is taken into account.

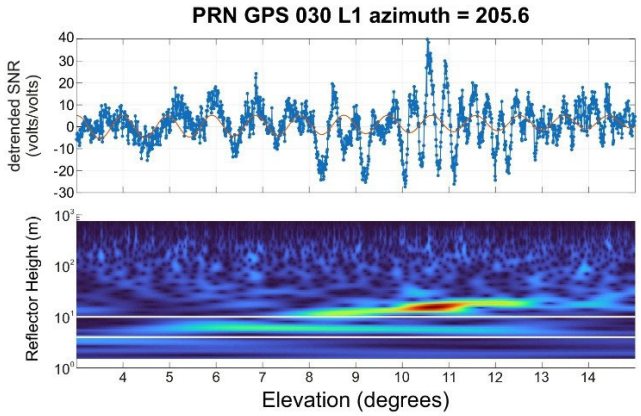


FIGURE 2. (Top) Detrended SNR and (Bottom) its continuous wavelet transform for an arc of GPS PRN 30 on the L1 signal at HNLC, recorded at an azimuth near 205.6 degrees. A contribution near the expected water level height is present across the arc, while a stronger contribution between about 8 and 13 degrees in elevation is consistent with a reflection from the sloping roof.

The mask cannot act on this arc in any useful way. Discarding it removes a valid water observation, and retaining it keeps the roof contribution, which is summed with the water reflection at the antenna before anything is recorded. In the terms of Section II-A, the roof produces a coherent but elevation dependent term whose power spreads across the spectrum of the arc, lowering the prominence of the water peak without forming a separable feature.

Figure 2 shows one arc. To establish that the effect is systematic rather than anecdotal, 292 days of HNLC observations from 2022 were processed and each arc was classified by whether it crosses the predicted roof footprint of Figure 1 (bottom). Of 11918 GPS L1 arcs, after removal of maxima lying at the edges of the 3.5 to 30 m height search interval, 3414 fall inside the predicted footprint and 8504 outside it. Arcs inside the footprint return a median PBNR of 3.03, with a bootstrap interval of 3.00 to 3.07, against 4.29 with an interval of 4.28 to 4.32 outside. The retrieved heights separate in the same way. Outside the footprint 77% of the arcs return a height between 4.5 and 7.0 m, the range expected for the water surface at this antenna, while inside the footprint 25% do, the remainder returning larger heights consistent with the roof. The two groups come from the same station, the same receiver and the same azimuth mask, and differ only in whether the geometry places a roof reflection inside the arc. The contamination is therefore measurable across the record and confined to the sector predicted from the roof geometry.

What would resolve the situation is not a different sector but a receiving element that attenuates arrivals from the roof direction before the summation, which is the property developed in the next section.

III. DIRECTIONAL ANTENNA DESIGN

This section describes the geometry of the antenna, its fabrication by additive manufacturing, its measured return loss, and its angular response obtained from electromagnetic simulation. No anechoic chamber was available, so the radiation pattern reported here is a design prediction and the field experiment described in the following sections is what tests it; the return loss, however, was measured on the fabricated antenna.

A. DESIGN AND FABRICATION

The requirement set out above concerns the shape of the antenna response instead of its absolute gain. Suppression of arrivals from the rear hemisphere is the property that a mask cannot provide, and it has to be obtained without narrowing the response to the point where the interference pattern is lost. A dual ridged horn antenna (DRHA) satisfies both conditions. The flaring aperture directs the response towards the boresight direction and the conducting walls attenuate arrivals from behind, while the ridges lower the cutoff frequency of the guiding structure and allow operation over a wide frequency range with an aperture of moderate size. The geometry is also well suited to fabrication by additive manufacturing, since it consists of planar and linearly flaring surfaces that can be printed as a single piece.

The antenna is shown in Figure 3 together with the receiver electronics and the data acquisition arrangement. Its structure consists of a base (1), a lower section (2) and a horn section (3), bounded by closed sidewalls (4) and by bridges (5) connecting them. Two ridges (6) of varying width extend from the base to the sidewalls. A connector (7) is mounted at the base for the antenna feed, with an inner conductor (8) as the live end and an outer conductor serving as the ground terminal.

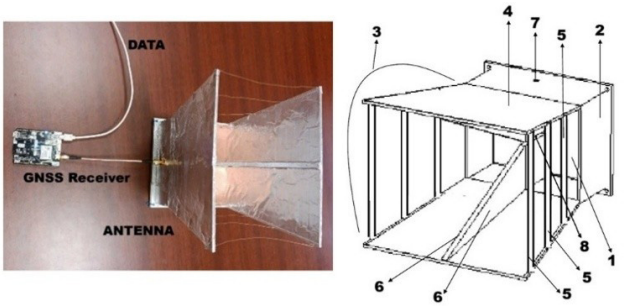


FIGURE 3. (Left) The fabricated antenna with the receiver electronics and the data acquisition arrangement, (Right) skeleton structure of the horn antenna model with the numbered components.

The antenna was designed in CST Microwave Studio, which provides full wave electromagnetic simulation and parametric optimization of the geometry [31]. The inner base measures $W_1 = 130$ mm by $H_1 = 100$ mm. From the base the structure continues as a straight section of length $L_1 = 50$ mm, followed by a linearly flaring horn section of length $L_2 = 160$ mm, so that the aperture measures $W_2 = 186$ mm by $H_2 = 152$ mm. Two ridges extend from the base towards the aperture with a width of $W_3 = 5$ mm and a maximum height of $H_3 = 55$ mm. A back cover of the same dimensions as the base and 3 mm in thickness encloses the lower end, and a SubMiniature Version A connector is mounted at the base. In place of continuous solid sidewalls, three evenly spaced rows of 3 mm annealed copper wire were stretched along the sides, an arrangement that has been reported to preserve horn antenna performance while reducing weight [32], [33]. The wire rows were drawn in the CST model with the geometry used in fabrication, and the conducting surfaces were assigned finite conductivity metal rather than a perfect electric conductor, annealed copper for the wires and aluminum for the coated surfaces. The geometry and the principal dimensions are shown in Figure 4.

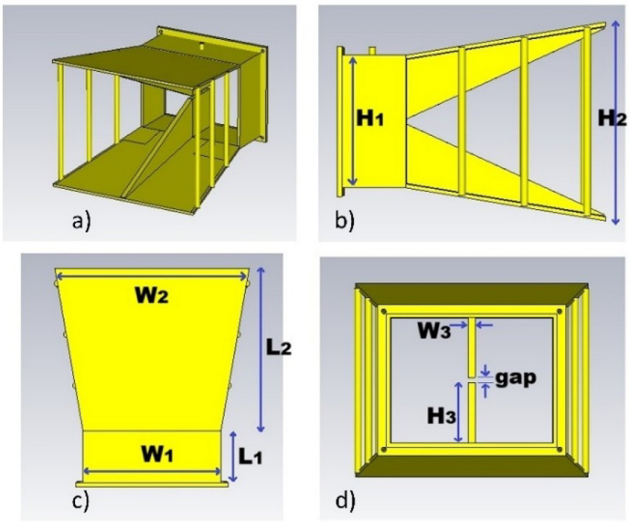


FIGURE 4. Key views and dimensions of the designed antenna. (a) Perspective view showing the ridges and the wire sidewalls, (b) side view with the base height H_1 and the aperture height H_2, (c) top view with the base width W_1, the aperture width W_2, the straight section length L_1 and the flaring section length L_2, (d) view along the antenna axis showing the ridge width W_3, the maximum ridge height H_3 and the gap between the two ridges.

The antenna was fabricated by Fused Deposition Modeling using Polylactic Acid filament. The printed structure is a dielectric and requires a conducting surface, which was obtained by covering the outer surface with household aluminum foil of 0.01 mm thickness, affixed with an adhesive. The foil thickness of 0.01 mm corresponds to approximately five skin depths at L1, so the conducting layer is electrically sufficient at the frequencies of interest. The same combination of PLA printing and metallic foil coating has been used previously for microwave components at comparable frequencies [21], [22], [34]. Fabrication by

additive manufacturing places the cost of the antenna well below that of a machined metal horn of the same geometry, and the complete assembly including the antenna, the receiver board and the connecting cable weighs less than 1.5 kg. The horn was printed with a 0.2 mm layer height, 90 percent infill and 1 mm wall thickness in about 16 h. The material cost, comprising roughly 200 g of PLA filament, the SMA connector, aluminum foil, copper wire and adhesive, is below 10 USD, far below the cost of geodetic-grade equipment.

B. SIMULATED ANGULAR RESPONSE AND MEASURED RETURN LOSS

The angular response of the antenna was obtained from the full wave model described above, and the pattern quantities reported here are simulation outputs; the return loss below is a measurement.

Figure 5 shows the simulated radiation patterns in the azimuth and elevation planes at L1. The response is concentrated towards the boresight direction, with a simulated directive gain of 9 dB. In the azimuth plane the gain decreases progressively away from boresight, and the mean level over the rear hemisphere is approximately 22 dB below the boresight value. This asymmetry is the property the design is intended to provide. The first null beamwidth is approximately 145 degrees. A response of this width is a design requirement and not a residual feature of the geometry, since GNSS-IR operates on the interference between the direct and the reflected signal and both components have to be received. A narrower pattern would suppress one of the two over part of the elevation range and the interference term would be lost.

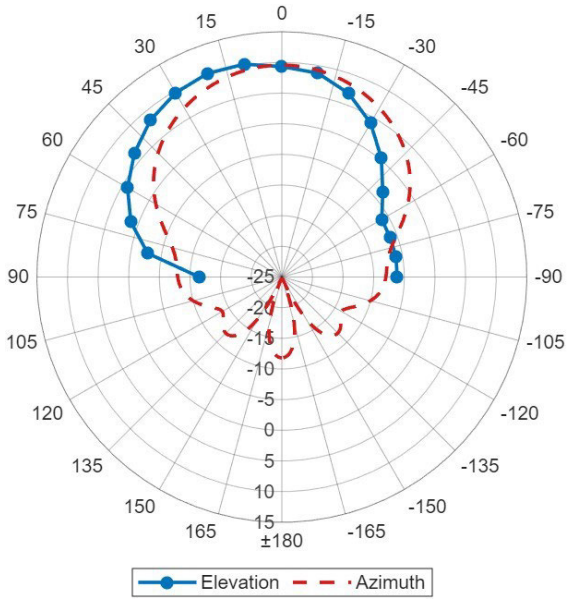


FIGURE 5. Simulated radiation patterns of the antenna at L1 in the azimuth and elevation planes.

The return loss is shown in Figure 6, measured on the fabricated antenna with a PicoVNA 106 vector network analyzer over 1 to 2 GHz following a SOLT calibration, and plotted against the simulation. The measured curve remains below −10 dB across the whole band. At the L2 band (1227.60 MHz) it reaches −12.6 dB against −12.5 dB in simulation, and at the L1 band (1575.42 MHz) −11.9 dB against −11.5 dB, so the fabricated antenna is matched in both bands, covering the three constellations used in the field experiment, GPS L1, GLONASS L1 and BeiDou B1I. Above 1600 MHz the measured match improves beyond the simulated value, in a region outside the bands used here. The return loss characterizes the input match of the fabricated antenna and does not bear on the radiation pattern, which remains a simulation output.

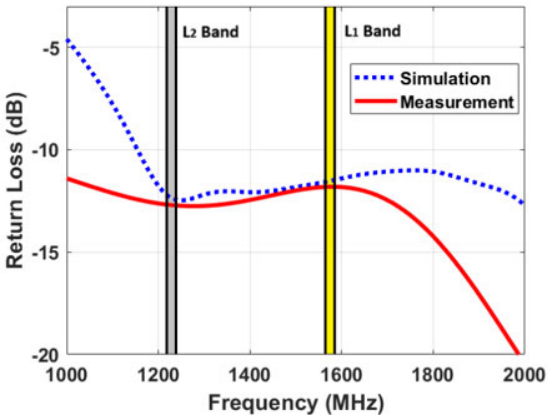


FIGURE 6. Return loss of the antenna: simulated (dotted) and measured with a vector network analyzer (solid). The L1 and L2 bands are shaded.

The simulated axial ratio exceeds 3 dB, so the antenna is linearly polarized. Direct GNSS signals are right hand circularly polarized, whereas the polarization of the reflected component depends on the surface and on the elevation angle and may be of either circular sense [38]. A circularly polarized antenna therefore receives the reflected component with an efficiency that varies with elevation angle and surface, whereas a linearly polarized aperture receives either circular sense with a fixed 3 dB mismatch. The direct and the reflected components are attenuated alike, so the absolute SNR is about 3 dB lower than with a matched circular antenna, while the ratio of the interference term to the direct level, and the frequency content that carries the height, are unaffected. Linear polarization is therefore not a limitation for reflectometric use.

In the field experiment the antenna is mounted horizontally with the boresight directed towards north, so that the boresight corresponds to zero azimuth at the horizon. Together with the pattern in Figure 5, this arrangement gives a definite expectation for the recorded data. Arcs associated with the sector around north should carry an interference term of high relative strength at the height of the reflecting surface, while arcs associated with the rear hemisphere should show no comparable concentration at that height. The field experiment

described below examines whether this is what the recorded data show.

IV. FIELD EXPERIMENT

The expected angular behavior is a property of the recorded data, and a field installation can test it. The antenna was deployed next to a fixed reflecting surface and operated with a low-cost receiver. A commercial antenna was connected to the same receiver and observed at the same site, so that the two configurations differ in the angular response of the receiving element and in little else. This section describes the site and the instrumentation, the processing applied to the observations, and the scope of the comparison.

A. SITE, INSTRUMENTATION, AND OBSERVATION SESSIONS

The experiment was carried out on the campus of the Of Technology Faculty of Karadeniz Technical University, Trabzon, Türkiye, at 40°55′ 48.4N and 40°16′ 35.7E. The antennas were mounted on a metal fence at the edge of the site. The target direction is north, where the ground below the antenna forms the reflecting surface of interest. That surface is not homogeneous: a paved walkway extends to 1.5 m from the installation, concrete from 1.5 to 7.5 m, and grass beyond that for a further 13 m. To the south, at a horizontal distance of 4 m, the installation faces the perimeter fence of an astroturf pitch. The ground carrying the pitch lies 1.89 m above the target surface, and the fence is 4 m high with a mesh aperture of 5 to 6 cm, so its top edge stands 2.9 m above the antenna and subtends an elevation angle of approximately 36 degrees. Arrivals from that side do not correspond to the target surface and are not usable for the retrieval. Figure 7 gives the dimensioned geometry of the site and the mounting.

Both antennas were installed on the same fence. The DRHA was mounted horizontally with its boresight directed towards north, corresponding to zero degrees in azimuth, while the u-blox ANN-MB-00-00 multi-band patch active antenna was installed in its normal orientation, with its ground plane horizontal and its beam directed towards the zenith, as in conventional GNSS-IR practice. The reference configuration is therefore the standard zenith-looking installation with an azimuth mask, which is the practice the paper examines. The reflector height measured in situ is 2.99 m for the DRHA and 3.22 m for the u-blox antenna, the difference following from the reference plane adopted for each antenna, the aperture mid plane for the horn and the ground plane for the patch. Figure 8 shows the two installations.

A single low-cost multi-band receiver, a u-blox ZED-F9P, recorded the observations in both cases, connected to the antenna through a SubMiniature Version A connector and a coaxial cable of 1.5 m, and powered by a battery. The reference antenna is a u-blox ANN-MB-00-00 multi-band patch antenna, whose response is broad and weakly discriminating in azimuth compared with that of the horn, which is the property under test.

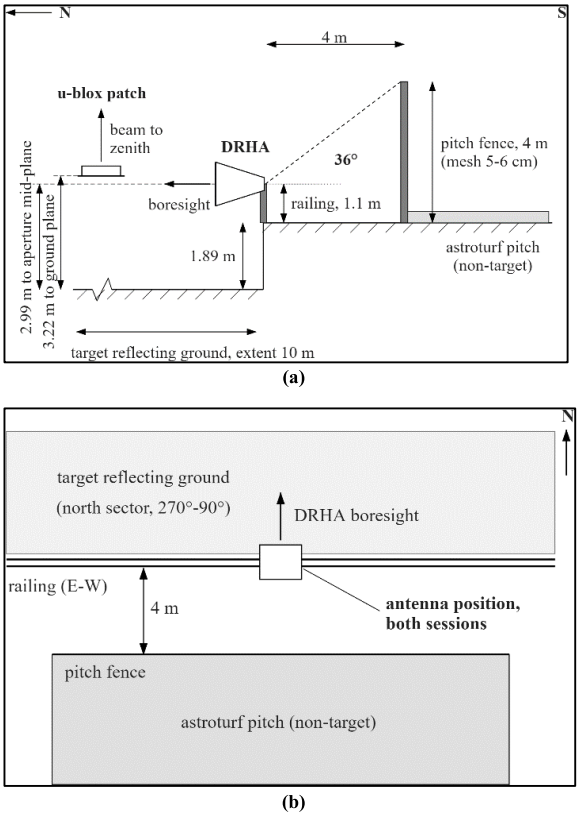


FIGURE 7. Dimensioned geometry of the field site. (a) Elevation, section looking east, with north to the left. The antennas are mounted on a railing 1.1 m above a level that stands 1.89 m above the target surface; the DRHA aperture mid-plane is at 2.99 m and the patch ground plane at 3.22 m. The perimeter fence of the astroturf pitch, 4 m to the south and 4 m high, subtends an elevation angle of approximately 36 degrees at the antenna. The two antennas are drawn side by side for clarity; the sessions were consecutive at the same point. (b) Plan view. Dimensions measured in situ.



FIGURE 8. Field installation at the Of Technology Faculty campus. (Left) The DRHA mounted horizontally with the boresight directed towards north, (Right) the reference u-blox ANN-MB-00-00 antenna in its normal zenith-up orientation at the same location.

The two sessions were recorded consecutively, since a single receiver was used. The DRHA was observed over

a full day on DoY 116 of 2026 (26 April), and the u-blox antenna over an interval of approximately 24.8 hours spanning DoY 114 and 115 (24 and 25 April). Both sessions therefore cover a complete repetition of the satellite geometry. Observations from three constellations were processed, GPS, GLONASS, and BeiDou, using signals in the L1 band. Only L1 observations are available from the two sessions, so the second matched band of the antenna is not exercised here.

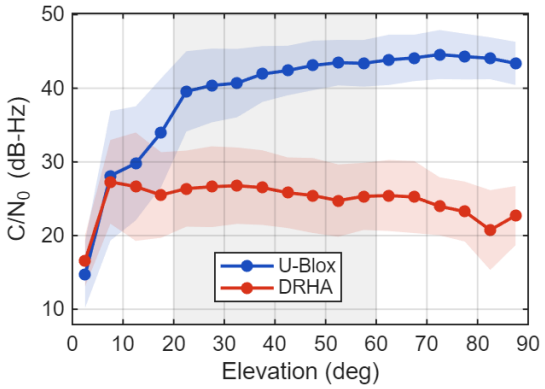


FIGURE 9. Mean L1 C/N_0 as a function of elevation angle for the two installations, computed over all epochs within the 270 to 90 degree azimuth sector in 5 degree bins. Shaded bands give one standard deviation. The gray area marks the 20 to 60 degree band used in the retrievals.

Figure 9 gives the mean L1 C/N0 as a function of elevation angle for the two installations within the azimuth sector used in the retrievals. Over the 20 to 60 degree band the u-blox antenna received between 39.6 and 43.5 dB-Hz and the DRHA between 24.8 and 26.8 dB-Hz; over the full sessions the receiver tracked 73 satellites with the u-blox antenna and 54 with the DRHA. Within the quality controlled arcs of Table 2 the median C/N0 is 44.0 dB-Hz for the u-blox antenna and 27.1 dB-Hz for the DRHA. The difference in level is consistent with the integrated low noise amplifier of the u-blox antenna, which the passive DRHA does not have. Both installations recorded usable signal across the retrieval band.

B. SNR DATA PROCESSING

The two data sets were processed with an identical chain, so that the recorded observations are the only quantity that differs between the two configurations. This subsection states each step in detail required to repeat it.

Observations were organized into satellite arcs, where an arc is a continuous tracking segment of one satellite on one signal, delimited by a change of sign in the elevation rate and by data gaps longer than 1 hour. Within the quality controlled arcs, no u-blox arc contains a gap longer than 125 s and 98 percent of the DRHA arcs contain no gap longer than 10 min. Arcs were restricted to elevation angles between 20 and 60 degrees. The band was chosen so that the specular footprint remains on the target surface. By Equation (5), elevations of 60 and 20 degrees place the specular point at 1.7 m and 8.2 m from the antenna respectively, spanning the concrete area that extends from 1.5 to 7.5 m and forms the bulk of that surface. Above 60 degrees the footprint moves onto the paved walkway immediately below the installation, and below 20 degrees it moves progressively into the grass beyond 7.5 m, whose effective reflecting plane sits within the vegetation rather than at the ground. The coastal case of Section II-B differs because a water surface extends far beyond the specular points of any retained arc, so the band there can be placed at low elevation angles without the footprint leaving the target, which is why the arcs there span 3 to 15 degrees. For the reflector height retrievals an azimuth restriction of 270 to 90 degrees was applied as well, retaining the hemisphere that contains the target surface. The same restriction was applied to both data sets, so the comparison is between a conventional antenna with an azimuth mask and a directional antenna with the same azimuth mask, and any remaining difference is a property of the receiving element and not of the arc selection. The retained band also fixes the height resolution of the estimator. Over 20 to 60 degrees $\Delta(sinE) = 0.524$, so Equation (6) gives $\Delta h \approx 0.18$ m at L1, of the same order as the median absolute deviation of 0.226 m reported in Section V-B for the DRHA. As stated in Section II-A, this limit concerns the separation of two contributions and not the location of a single dominant peak, which can be determined to a small fraction of Δh.

Recorded SNR values were converted to linear amplitude units, and the direct signal contribution was removed by fitting a second order polynomial in elevation angle to each arc and subtracting it, which gives the dSNR data. The Lomb Scargle periodogram (LSP) of the dSNR data was then computed against $\sin E$ [35], [36], [37] and converted to the height domain through Equation (2), using the carrier wavelength of each satellite and signal, with the frequency division channel number applied for each GLONASS satellite. The spectrum was computed from 0.1 to 10.0 m with a grid spacing of 0.001 m, which oversamples the height resolution given by Equation (6) so that the position of an isolated maximum is not limited by the grid. The reflector height retrieved from an arc is the position of the largest maximum in its spectrum.

The prominence of that maximum relative to the rest of the spectrum is the quantity through which the behavior described in Section II-A becomes measurable, since a contribution that does not follow Equation (1) is distributed across the spectrum instead of forming a maximum of its own. It is expressed as the peak-to-background noise ratio,

$$PBNR = \frac{P(h)}{\frac{1}{N}\sum_{i=1}^{N} P(h_i)} \tag{7}$$

where P is the spectral amplitude and N is the number of grid heights. The ratio is dimensionless and independent of the absolute amplitude of an arc, which makes it comparable between arcs recorded through different antennas.

An arc enters the reported statistics when it contains at least 20 observations, spans at least 10 degrees in elevation, reaches a PBNR above 3, and has its maximum further than

0.2 m from either end of the height grid. The last condition removes maxima that are an edge artifact of the search interval rather than a resolved peak.

The two sessions were recorded on different days, so arc identifiers are not comparable across them. A subset of arcs was therefore paired between the two configurations, matching arcs of the same GPS satellite and the same signal whose time of day windows overlap by at least half of the shorter arc. Quality control is applied before matching, so a rejected arc cannot occupy the position of a usable one. Only GPS is paired, because the GPS ground track repeats on a sidereal day and a given satellite therefore traces nearly the same path across the sky at the same time of day, while the remaining constellations do not repeat in this way. The matched subset is used for PBNR alone. It answers whether the same observing geometry produces a more prominent spectral peak through one antenna than through the other, and reflector height statistics are reported over all quality controlled arcs.

Two further products characterize the angular response. In the first, a continuous wavelet transform was applied to the dSNR data of each arc on a height grid of 0.1 m, and the coefficient magnitude at the height of the target surface was extracted for every elevation sample and mapped onto a polar plot in azimuth and elevation. In the second, arcs were grouped into eight sectors of 45 degrees by their circular median azimuth, the spectrum of each arc was interpolated onto a common height grid, and the spectra within a sector were averaged. Each set of curves was divided by the largest value reached by that configuration across all sectors, which preserves the relative strength between sectors while keeping the two configurations comparable.

Uncertainty in the reported statistics is quantified by a nonparametric bootstrap: within each antenna and constellation group, arcs are resampled with replacement, the median and the median absolute deviation are recomputed on each of 2000 replicates, and the 2.5th and 97.5th percentiles of the replicate distribution give a 95% confidence interval. The bootstrap makes no distributional assumption, which is appropriate for samples of a few tens of arcs. The PBNR difference over the matched pairs is tested with the Wilcoxon signed-rank statistic on the within-pair differences, since the pairing removes the between-arc geometric variability.

Processing was carried out with GIRAS, an open-source MATLAB toolbox for GNSS-IR analysis [12], together with routines written for this study for the arc processing, the matched arc comparison, and the two angular products. Table 1 lists the processing parameters.

TABLE 1. Processing parameters.

Parameter	Value
Signals	GPS L1 C/A, GLONASS L1 C/A, BeiDou B1I
Elevation range	20° to 60°
Azimuth range, h retrievals	270° to 90°
Azimuth range, angular characterization	unrestricted
Segment gap threshold	1 h
Detrending	Polynomial, order 2
LSP h-search interval	0.1 to 10.0 m
LSP h-grid spacing	0.001 m
Min. obs. per arc	20
Min. elev. span per arc	10°
Min. PBNR	3
Peak distance from grid edge	0.2 m
Azimuth sector width	45°
Wavelet h-resolution	0.1 m

C. SCOPE OF THE EXPERIMENT

The unit of analysis is the individual satellite arc and not the observation session, since each arc constitutes an independent spectral estimate with its own geometry and a single session provides several tens of them for each configuration. This design follows from the quantity under examination. An antenna radiation pattern is fixed, and the satellite geometry repeats on close to a sidereal day, so that the recorded data sample a deterministic angular response. The experiment accordingly examines whether the angular behavior predicted in Section III-B is present in the recorded data at a single site, and the results are reported on that basis.

The time separation between the two sessions has two consequences. A single receiver observed the two antennas consecutively, so receiver-side conditions are common by construction and only the receiving element differs, at the cost of excluding simultaneous operation. The surface state was not measured independently for either period, and a change in ground reflectivity between DoY 114–115 and DoY 116 would alter the recorded amplitudes; a change that is uniform in azimuth, however, scales all sectors of one configuration alike and cancels in the north-to-south ratio of Section V-A, while the height retrievals depend on the frequency of the interference term rather than on its amplitude.

V. RESULTS

Processing the two data sets over the retained azimuth sector produced 156 arcs for the u-blox antenna and 96 arcs for the DRHA. Of these, 67 and 49 respectively satisfied the quality control conditions of Section IV-B, corresponding to pass rates of 43% and 51%. The difference in the number of arcs follows from the signal level shown in Figure 9: the passive, linearly polarized DRHA delivers a C/N0 some 17 dB below that of the active patch antenna, so satellites are acquired over a shorter part of their passes and some passes yield no trackable segment at all. That the DRHA nonetheless returns the higher proportion of usable arcs is the first indication of the effect examined below. The two sessions also differ slightly in length, so the arc counts are not directly proportional to the observing time. The results below are reported first over the whole sky, then over the arcs retained in the target sector, and finally over the subset of arcs paired between the two configurations.

A. ANGULAR RESPONSE

The two products in this subsection describe where in the sky the interference term associated with the target surface is present, and they were computed without the azimuth restriction so that the whole sky is represented.

Figure 10 shows the magnitude of the wavelet coefficient at the height of the target surface, sampled for every elevation step of every arc and plotted against the azimuth and the elevation angle of the satellite. The sampling height is the value measured in situ for each installation, 3.22 m for the u-blox antenna and 2.99 m for the DRHA, since the reference plane of each antenna sits at a different height on the railing, the ground plane for the patch antenna and the aperture mid plane for the horn, as shown in Figure 7. Each panel is normalized by its own largest value, so the comparison is between the distributions across the sky and not between absolute levels. This is appropriate given that the two configurations differ in the gain of the receiving element.

With both antennas the strongest contributions come from the sector containing the target surface, as expected. The two distributions differ in what is recorded from the remaining directions. With the u-blox antenna the interference term at the height of the target surface is present across the southern half of the sky at an appreciable fraction of the level reached in the north, although no target surface lies in that direction and the term cannot originate there at that height. With the DRHA the southern half is reduced to a low and largely uniform level, and the contributions are concentrated in the sector around the antenna boresight, where they also extend to lower elevation angles than with the u-blox antenna.

The ratio between the median coefficient magnitude over the northern half of the sky, from 270 to 90 degrees in azimuth, and the median over the southern half is 2.5 for the u-blox antenna and 5.6 for the DRHA. The contrast between the sector containing the target surface and the sector that does not is therefore more than twice as large with the directional antenna. This ratio is formed within each configuration and is independent of the absolute gain, so it is comparable between the two.

Neither panel shows an abrupt boundary between the two regions. The response falls off gradually with azimuth, as a radiation pattern does and as a threshold applied to a coordinate would not. An azimuth mask is exactly such a threshold, and applied to the same data would set the southern arcs aside entirely while leaving the recorded contribution from those directions inside every retained arc, which is the distinction developed in Section II-A.

Figure 11 shows the mean Lomb Scargle amplitude spectrum in each of the eight azimuth sectors, normalized for each configuration by the largest value it reaches across all sectors.

In the four sectors facing the target surface, from 270 to 90 degrees, both configurations carry a maximum near a reflector height of 3 m. With the DRHA this maximum is narrow and dominates its sector, reaching the largest value recorded for that configuration in the sector from 0 to 45 degrees. With the u-blox antenna amplitude of a similar order is spread across the range below 2 m and above 3 m, so the height of the target surface is not clearly separated from the rest of the spectrum.

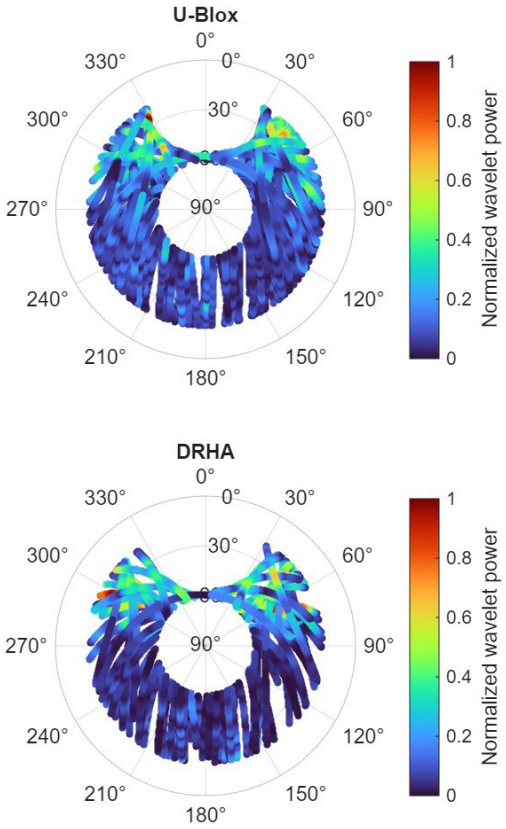


FIGURE 10. Normalized wavelet coefficient magnitude at the height of the target surface, plotted against satellite azimuth and elevation angle. (Top) U-blox antenna, sampled at 3.22 m, (Bottom) DRHA, sampled at 2.99 m. Each panel is normalized by its own maximum.

The four sectors facing away from the target surface separate the two configurations more sharply. With the u-blox antenna they carry a pronounced maximum below 1 m, which in the sector from 180 to 225 degrees is the largest value recorded for that antenna anywhere in the sky. The strongest mean spectral feature obtained with the u-blox antenna therefore comes from a direction in which no target surface is present. With the DRHA the same sectors are close to flat at every height.

A contribution below 1 m is present in the northern sectors as well, weaker with the DRHA than with the u-blox antenna. Its origin is examined in Section VI. It is recorded within the arcs that an azimuth mask retains, so its weight in the spectrum is set by the angular response of the antenna rather than by the arc selection.

B. REFLECTOR HEIGHT AND PBNR STATISTICS

The retrievals here are obtained over the azimuth sector from 270 to 90 degrees, applied identically to both configurations, and over the arcs that satisfy the quality control

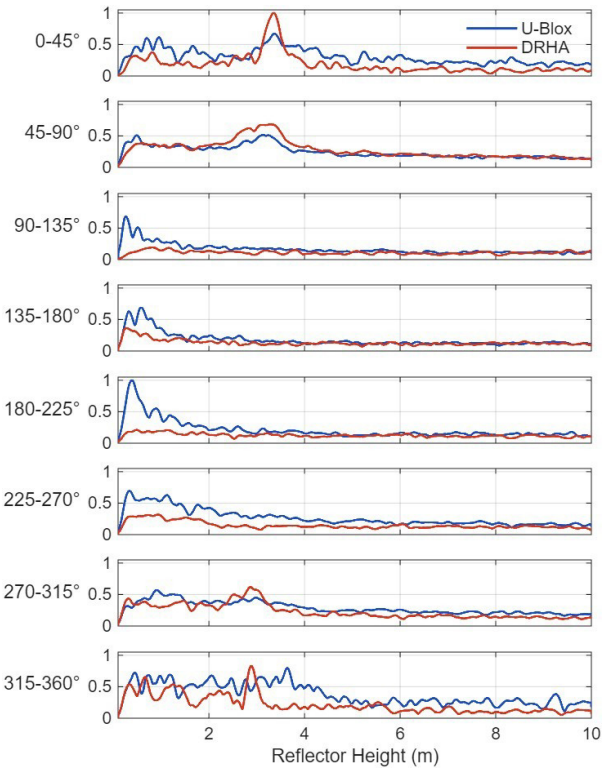


FIGURE 11. Normalized mean Lomb Scargle spectral amplitude per 45 degree azimuth sector for the DRHA and the u-blox antenna. S1C signals, elevation angles from 20 to 60 degrees, no azimuth restriction. The curves of each configuration are normalized by the largest value it reaches across all sectors.

conditions of Section IV-B. Table 2 lists the results for all constellations together and for each constellation separately. Because the target is a fixed surface, the in-situ height is a single time-invariant reference, and the RMSE against it is computed over all quality-controlled arcs of the session rather than as a time-resolved statistic.

TABLE 2. Reflector Height and PBNR Statistics for Quality Controlled Arcs in the 270 to 90 Degree Azimuth Sector over the Full Session of each Antenna (DRHA 24 h, U-Blox 24.8 h).

Ant.	Const.	n	h_{med} (m)	h_{MAD} (m)	h_{RMSE} (m)	PBNR med	PBNR MAD
U-Blox	GPS	29	2.754	0.626	1.650	3.88	0.35
	GLO	14	1.331	0.623	1.767	3.79	0.57
	BDS	24	1.666	1.244	1.689	3.66	0.37
	All	67	1.682	1.235	1.689	3.73	0.41
DRHA	GPS	19	2.992	0.231	0.596	4.89	0.68
	GLO	13	3.009	0.208	0.851	4.96	1.16
	BDS	17	2.873	0.217	0.614	4.87	0.98
	All	49	2.991	0.226	0.679	4.89	0.87

With the DRHA the median over all constellations is 2.991 m, in agreement with the 2.99 m determined in situ, and the median absolute deviation is 0.226 m and the RMSE against the in-situ height is 0.679 m. The three constellations return 2.992 m, 3.009 m, and 2.873 m, within 0.136 m of each other, with a median absolute deviation between 0.208 m and 0.231 m in every case. Three constellations observing the same surface through the same receiver therefore recover the same height, which shows that the agreement does not depend on any single constellation geometry. A spread of this order is expected at this site, since the specular point moves over several meters of ground as the elevation angle changes and the surface is neither flat nor uniform in its reflecting properties, so each arc samples a slightly different effective height.

The u-blox antenna does not reproduce this behavior. Its median over all constellations is 1.682 m, displaced by more than 1.5 m from the 3.22 m determined in situ for that installation, and its median absolute deviation of 1.235 m is more than five times the value obtained with the DRHA. The three constellations return 2.754 m, 1.331 m, and 1.666 m, spread over 1.423 m, and none of them approaches the in-situ value. The RMSE of 1.689 m against the in-situ height is dominated by arcs whose retrieved height lies far from the target, which is why the median absolute deviation is used as the primary dispersion measure throughout. Retrievals of this kind carry no usable information on the target surface, even though the same azimuth restriction was applied to both configurations.

The PBNR follows the same ordering with a smaller separation, with a median of 4.89 for the DRHA against 3.73 for the u-blox antenna, and the ordering holds for each constellation taken separately. The number of arcs also differs. The u-blox antenna produced 156 arcs over the retained sector, of which 67 satisfied the quality control, against 96 and 49 for the DRHA. The DRHA therefore returns fewer arcs and a higher proportion of usable ones, and those arcs recover the target surface consistently while the u-blox retrievals do not.

C. MATCHED ARC COMPARISON

Pairing the arcs between the two configurations gives 16 GPS pairs, each formed from the same satellite and signal observed over overlapping windows in the time of day, so that the geometry with respect to the target surface is common to both members of a pair.

Figure 12 compares the dSNR data and the spectra of one pair. The DRHA spectrum carries a single strong maximum near 3 m and reaches a PBNR of 6.4. The u-blox spectrum reaches 3.3, with several maxima of comparable amplitude spread over the height range and a dense group below 1 m, so the interference term at the target surface competes with contributions at other frequencies that the same arc also records.

Over the 16 pairs the median PBNR is 3.78 with a median absolute deviation of 0.41 for the u-blox antenna and 4.59 with 0.64 for the DRHA, and the ratio taken within each pair gives a mean gain of approximately 20% and a median gain of 12%. The DRHA member reaches the higher PBNR in 12 of the 16 pairs, the median within-pair difference

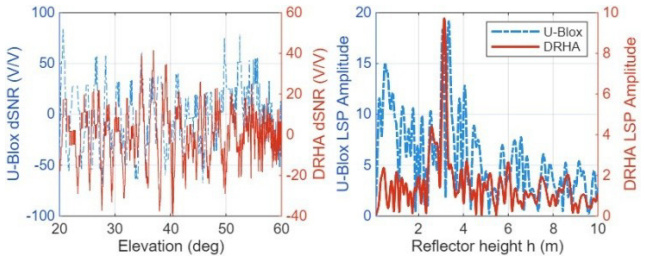


FIGURE 12. Detrended SNR and LSP for the matched G17 arc pair on the L1 C/A signal. (Left) Detrended SNR against elevation angle. (Right) LSP amplitude against reflector height. Each configuration is plotted on its own vertical scale.

is 0.455 with a 95 percent bootstrap interval from 0.034 to 1.406, and a two-sided Wilcoxon signed-rank test on the within-pair differences gives $p = 0.056$. The retrieved heights separate the two more widely, with a median of 2.884 m and a median absolute deviation of 0.319 m for the DRHA against 1.473 m and 1.062 m for the u-blox antenna.

VI. DISCUSSION AND CONCLUSION

The in-situ reflector height refers to the mid plane of the aperture, and the phase center of a horn shifts along the boresight axis, so in this horizontal mounting of the horn the shift does not enter the vertical distance under estimation and the associated uncertainty is bounded by the aperture half height of 76 mm. The median absolute deviation of approximately 20 cm instead reflects the surface. By Equation (5), with the in-situ height of 2.99 m, the specular point moves from 8.2 m to 1.7 m of horizontal distance as the elevation angle rises from 20 to 60 degrees, and the ground north of the installation is not homogeneous over that strip, with a paved walkway to 1.5 m, concrete from 1.5 to 7.5 m and grass beyond. Arcs near the lower limit of the retained band therefore sample a surface with a different reflection coefficient and an effective reflecting plane within the vegetation, and each arc returns a slightly different effective height.

The contribution at low reflector heights in Figure 11 is present mainly with the u-blox antenna, and the non-target reflector at this site can be described precisely. The perimeter fence described in Section IV-A intercepts every southward arrival over the lower part of the retained band. Its mesh aperture of 5 to 6 cm is roughly a third of the L1 wavelength, so the screen behaves as an approximately continuous conductor, the same principle that allows the wire grid sidewalls of the horn to perform as solid walls [32], [33]. A large, close, strongly reflecting structure subtending a wide solid angle is exactly the case identified in Section II-A. Together with the railing on which the antennas are mounted, it is the most plausible source of the sub-meter feature that dominates the southern sectors of Figure 11 with the u-blox antenna. Because the two antennas occupied the same point on the railing in succession, the near-field environment was common to both sessions. Restricting the azimuth manually does not remove this contribution, as the same mask was applied to both data sets and it remains in the u-blox spectra. Suppressing the arrivals from that direction at the aperture does remove it, which is what the DRHA data show.

Two mechanisms act in this experiment and should be distinguished. With its boresight at the horizon and a simulated first null beamwidth of approximately 145 degrees, the DRHA attenuates the direct signal from higher elevation satellites relative to the near horizon reflected component, altering the direct to reflected balance in the manner that side looking installations exploit in the elevation domain [28], [29]. Part of the PBNR improvement reported in Section V is attributable to this known mechanism. A pattern that varies with elevation only, however, strengthens every arrival near the horizon alike, the target surface and the fence behind the antenna included, and cannot change which reflector dominates the spectrum. The displacement of the u-blox median by more than 1.5 m and the five-fold increase of its median absolute deviation are the signature of a competing reflector dominating a large fraction of the arcs, and Figure 11 locates that reflector in the southern sectors. Its dominance with one antenna and its suppression with the other at the same elevation angles can only follow from the difference in the azimuth response. The retained sector of 270 to 90 degrees is essentially the forward hemisphere of the horn, so the antenna adds no azimuth discrimination among the retained arcs; its action is the suppression of arrivals from behind, which is the property required in Section II-A. A quantitative partition of the two contributions would require the polarimetric forward model of [38] evaluated with a measured pattern and is left to future work.

The bootstrap intervals quantify how well each configuration determines the surface. Overall quality controlled arcs the 95 percent interval of the DRHA height median is 0.25 m wide and contains the in-situ value, while the interval of the u-blox median is 1.66 m wide and spans most of the range between the non-target feature and the target surface. The PBNR medians separate more cleanly, with intervals of 3.66 to 3.92 for the u-blox antenna and 4.41 to 5.39 for the DRHA that do not overlap. The separation between the two configurations is larger in the retrieved heights than in the PBNR, and the two are consistent. Retrieval is an argmax operation, so when non-target contributions raise the background and support a competing maximum of comparable amplitude, a modest reduction in relative peak prominence is enough to hand the maximum to a different feature. The PBNR medians are also conditional on the screening, since arcs below the threshold of 3 never enter the statistics, and the u-blox median of 3.73 sits close to that threshold by construction. A modest difference in median PBNR and a categorical difference in retrieved height therefore measure different things, how far the surviving peaks stand above the background and which peak wins.

The experiment was designed as a proof of concept, and its scope is stated accordingly. The comparison rests on one site, two consecutive single day sessions on a single receiver, and

L1 observations, and the pattern of the antenna is a simulation output that no chamber measurement accompanies, although the return loss of the fabricated antenna has been measured (Figure 6). Within that scope the recorded data show the predicted behavior, a concentration of the interference term in the boresight sector, a low and nearly uniform response behind the antenna, and retrievals that recover the surveyed height with three constellations, while the patch antenna in its conventional zenith-looking orientation under the same mask does not. The two sessions were recorded on different days, so a change in ground reflectivity between them cannot be excluded; a change of this kind alters the amplitude of the interference term, whereas the height retrievals depend on its frequency. What remains open is performance over time and over sites, in particular at coastal stations of the kind described in Section II-B, where the target is water and the non-target reflector is a building. A deployment of this type, together with simultaneous operation on two receivers, chamber characterization of the fabricated antenna, and use of the second matched band, is the natural continuation of this work.

Azimuth masking selects arcs by the computed satellite direction, while the antenna weights each contribution by its direction of arrival before the summation at the aperture, and only the second of these acts on what is recorded. This work examined that distinction in the field, with a 3D printed dual ridged horn deployed at a site with a fixed reflecting surface and compared against a patch antenna in its conventional orientation under the same mask and processing chain. The directional antenna recovered the surveyed reflector height with three constellations and confined the response to the boresight sector, while the patch antenna returned retrievals dominated by non-target surfaces that the mask could not exclude. Hardware level angular filtering is therefore a workable and low-cost complement to masking at sites where the target surface cannot be isolated in the data domain.

ACKNOWLEDGMENT

The authors thank the NOAA Center for Operational Oceanographic Products and Services for maintaining the HNLC station and the Honolulu tide gauge records used in this study.

REFERENCES

[1] M. Martin-Neira, "A passive reflectometry and interferometry system (PARIS): Application to ocean altimetry," *ESA J.*, vol. 17, no. 4, pp. 331–355, 1993.

[2] E. E. Small, K. M. Larson, and J. J. Braun, "Sensing vegetation growth with reflected GPS signals," *Geophys. Res. Lett.*, vol. 37, no. 12, p. 12401, Jun. 2010, doi: 10.1029/2010gl042951.

[3] M. Ozeki and K. Heki, "GPS snow depth meter with geometry-free linear combinations of carrier phases," *J. Geodesy*, vol. 86, no. 3, pp. 209–219, Mar. 2012, doi: 10.1007/s00190-011-0511-x.

[4] K. M. Larson, E. E. Small, E. D. Gutmann, A. L. Bilich, J. J. Braun, and V. U. Zavorotny, "Can we measure snow depth with GPS receivers?" *Geophys. Res. Lett.*, vol. 36, no. 17, p. 17502, Sep. 2009, doi: 10.1029/2009gl039430.

[5] K. M. Larson, E. E. Small, E. Gutmann, A. Bilich, P. Axelrad, and J. Braun, "Using GPS multipath to measure soil moisture fluctuations: Initial results," *GPS Solutions*, vol. 12, no. 3, pp. 173–177, Jul. 2008, doi: 10.1007/s10291-007-0076-6.

[6] K. M. Larson and F. G. Nievinski, "GPS snow sensing: Results from the EarthScope plate boundary observatory," *GPS Solutions*, vol. 17, no. 1, pp. 41–52, Jan. 2013, doi: 10.1007/s10291-012-0259-7.

[7] C. Roesler and K. M. Larson, "Software tools for GNSS interferometric reflectometry (GNSS-IR)," *GPS Solutions*, vol. 22, no. 3, p. 80, Jul. 2018, doi: 10.1007/s10291-018-0744-8.

[8] A. Martín, R. Luján, and A. B. Anquela, "Python software tools for GNSS interferometric reflectometry (GNSS-IR)," *GPS Solutions*, vol. 24, no. 4, p. 94, Oct. 2020, doi: 10.1007/s10291-020-01010-0.

[9] M. A. R. Fagundes, I. Mendonça-Tinti, A. L. Iescheck, D. M. Akos, and F. Geremia-Nievinski, "An open-source low-cost sensor for SNR-based GNSS reflectometry: Design and long-term validation towards sea-level altimetry," *GPS Solutions*, vol. 25, no. 2, p. 73, Apr. 2021, doi: 10.1007/s10291-021-01087-1.

[10] S. Zhang, J. Peng, C. Zhang, X. Nan, X. Chen, and B. Wang, "GiRsnow: An open-source software for snow depth retrievals using GNSS interferometric reflectometry," *GPS Solutions*, vol. 25, no. 2, p. 55, Apr. 2021, doi: 10.1007/s10291-021-01096-0.

[11] K. M. Larson, "Gnssrefl: An open source software package in Python for GNSS interferometric reflectometry applications," *GPS Solutions*, vol. 28, no. 4, p. 165, Oct. 2024, doi: 10.1007/s10291-024-01694-8.

[12] C. Altuntas and N. Tunalioglu, "GIRAS: An open-source MATLAB-based software for GNSS-IR analysis," *GPS Solutions*, vol. 26, no. 1, p. 16, Jan. 2022, doi: 10.1007/s10291-021-01201-3.

[13] C. C. Chew, E. E. Small, K. M. Larson, and V. U. Zavorotny, "Vegetation sensing using GPS-interferometric reflectometry: Theoretical effects of canopy parameters on signal-to-noise ratio data," *IEEE Trans. Geosci. Remote Sens.*, vol. 53, no. 5, pp. 2755–2764, May 2015, doi: 10.1109/TGRS.2014.2364513.

[14] K. M. Larson, J. J. Braun, E. E. Small, V. U. Zavorotny, E. D. Gutmann, and A. L. Bilich, "GPS multipath and its relation to near-surface soil moisture content," *IEEE J. Sel. Topics Appl. Earth Observ. Remote Sens.*, vol. 3, no. 1, pp. 91–99, Mar. 2010, doi: 10.1109/JSTARS.2009.2033612.

[15] K. M. Larson, E. E. Small, E. D. Gutmann, A. L. Bilich, J. J. Braun, and V. U. Zavorotny, "Use of GPS receivers as a soil moisture network for water cycle studies," *Geophys. Res. Lett.*, vol. 35, no. 24, p. 24405, Dec. 2008, doi: 10.1029/2008gl036013.

[16] C. Altuntas and N. Tunalioglu, "Feasibility of retrieving effective reflector height using GNSS-IR from a single-frequency Android smartphone SNR data," *Digit. Signal Process.*, vol. 112, May 2021, Art. no. 103011, doi: 10.1016/j.dsp.2021.103011.

[17] C. Altuntas, N. Tunalioglu, and T. Ocalan, "Datum alignment between GNSS-IR sea level estimations and tide gauges in Türkiye: A vertical local tie approach," *Mar. Geodesy*, vol. 48, no. 1, pp. 2–20, Jan. 2025, doi: 10.1080/01490419.2024.2402008.

[18] C. Altuntas, M. C. Iban, E. Şentürk, U. M. Durdag, and N. Tunalioglu, "Machine learning-based snow depth retrieval using GNSS signal-to-noise ratio data," *GPS Solutions*, vol. 26, no. 4, p. 117, Oct. 2022, doi: 10.1007/s10291-022-01307-2.

[19] C. Altuntas and N. Tunalioglu, "A systematic approach for identifying optimal azimuth and elevation angle masks in GNSS-IR: Validation through a sea level experiment," *GPS Solutions*, vol. 27, no. 4, p. 198, Oct. 2023, doi: 10.1007/s10291-023-01535-0.

[20] S. Sarjoghian, A. Alieldin, Y. Huang, C. Song, and R. Alrawashdeh, "A 3D-printed high-dielectric filled elliptical double-ridged horn antenna for biomedical monitoring applications," *IEEE Access*, vol. 7, pp. 94977–94985, 2019, doi: 10.1109/ACCESS.2019.2928629.

[21] B. Majumdar, D. Baer, S. Chakraborty, K. P. Esselle, and M. Heimlich, "Advantages and limitations of 3D printing a dual-ridged horn antenna," *Microw. Opt. Technol. Lett.*, vol. 58, no. 9, pp. 2110–2117, Sep. 2016, doi: 10.1002/mop.30026.

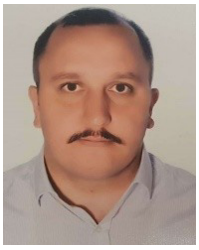
[22] Ö. Kasar, M. Geçin, and M. A. Gözel, "Design and implementation of a 3D printed RF power transceiver clamp to measure the water level in PVC water pipes," *Int. J. RF Microw. Comput.-Aided Eng.*, vol. 31, no. 5, p. 22644, May 2021, doi: 10.1002/mmce.22644.

[23] A. M. Kulkarni, G. Saini, S. S. Pattnaik, and R. A. Pardeshi, "3D printing in antenna design," in *3D Printing of Sensors, Actuators, and Antennas for Low-Cost Product Manufacturing*. Boca Raton, FL, USA: CRC Press, 2022, pp. 31–60.

[24] S. D. P. Williams, P. S. Bell, D. L. McCann, R. Cooke, and C. Sams, "Demonstrating the potential of low-cost GPS units for the remote measurement of tides and water levels using interferometric reflectometry," *J. Atmos. Ocean. Technol.*, vol. 37, no. 10, pp. 1925–1935, Oct. 2020, doi: 10.1175/jtech-d-20-0063.1.
[25] M. A. Karegar, J. Kusche, F. Geremia-Nievinski, and K. M. Larson, "Raspberry pi reflector (RPR): A low-cost water-level monitoring system based on GNSS interferometric reflectometry," *Water Resour. Res.*, vol. 58, no. 12, p. 2021, Dec. 2022, doi: 10.1029/2021wr031713.
[26] L. Chen, H. Chai, N. Zheng, M. Wang, and M. Xiang, "Feasibility and performance evaluation of low-cost GNSS devices for sea level measurement based on GNSS-IR," *Adv. Space Res.*, vol. 72, no. 11, pp. 4651–4662, Dec. 2023, doi: 10.1016/j.asr.2023.07.031.
[27] S. Rover and A. Vitti, "GNSS-R with low-cost receivers for retrieval of antenna height from snow surfaces using single-frequency observations," *Sensors*, vol. 19, no. 24, p. 5536, Dec. 2019, doi: 10.3390/s19245536.
[28] A. Santamaría-Gómez and C. Watson, "Remote leveling of tide gauges using GNSS reflectometry: Case study at Spring Bay, Australia," *GPS Solutions*, vol. 21, no. 2, pp. 451–459, Apr. 2017, doi: 10.1007/s10291-016-0537-x.
[29] C. Altuntaş and N. Tunalioğlu, "Retrieving the SNR metrics with different antenna configurations for GNSS-IR," *Turkish J. Eng.*, vol. 6, no. 1, pp. 87–94, Jan. 2022, doi: 10.31127/tuje.870620.
[30] Y. Lv, X. Gao, H. Jiang, F. Wang, and X. Wang, "Surface-dependent responses of GNSS SNR amplitude to rainfall events: Insights from simulation and field validation," *IEEE Access*, vol. 14, pp. 112553–112561, 2026, doi: 10.1109/ACCESS.2026.3715769.
[31] Dassault Systèmes. *CST Microwave Studio*. Accessed: Oct. 9, 2026. [Online]. Available: https://www.3ds.com/products-services/simulia/products/cst-studio-suite/
[32] B. Jacobs, J. W. Odendaal, and J. Joubert, "An improved design for a 1–18 GHz double-ridged guide horn antenna," *IEEE Trans. Antennas Propag.*, vol. 60, no. 9, pp. 4110–4118, Sep. 2012, doi: 10.1109/TAP.2012.2207043.
[33] S. Lin, S. Liu, Y. Zhang, and J. Jiao, "Analysis and experiment of a ridged horn antenna with metallic grid sidewalls," *Prog. Electromagn. Res. C*, vol. 96, pp. 27–41, 2019, doi: 10.2528/pierc19071504.
[34] Ö. Kasar and U. M. Durdağ, "Realization of a double-ridge horn antenna with 3D printing and aluminum coating study for 5G indoor applications," *Int. J. 3D Printing Technol. Digit. Ind.*, vol. 7, no. 3, pp. 499–504, Dec. 2023, doi: 10.46519/ij3dptdi.1365999.
[35] N. R. Lomb, "Least-squares frequency analysis of unequally spaced data," *Astrophys. Space Sci.*, vol. 39, no. 2, pp. 447–462, Feb. 1976, doi: 10.1007/bf00648343.
[36] J. D. Scargle, "Studies in astronomical time series analysis. II—Statistical aspects of spectral analysis of unevenly spaced data," *Astrophysical J.*, vol. 263, pp. 835–853, Dec. 1982, doi: 10.1086/160554.
[37] K. Hocke, "Phase estimation with the Lomb–Scargle periodogram method," *Ann. Geophys.*, vol. 16, no. 3, pp. 356–358, Mar. 1998.
[38] F. G. Nievinski and K. M. Larson, "Forward modeling of GPS multipath for near-surface reflectometry and positioning applications," *GPS Solutions*, vol. 18, no. 2, pp. 309–322, Apr. 2014, doi: 10.1007/s10291-013-0331-y.
[39] S. Farzaneh, K. Parvazi, and H. H. Shali, "GNSS-IR-UT: A MATLAB-based software for SNR-based GNSS interferometric reflectometry (GNSS-IR) analysis," *Earth Sci. Informat.*, vol. 14, no. 3, pp. 1633–1645, Sep. 2021, doi: 10.1007/s12145-021-00637-y.



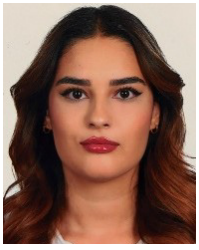
UTKAN MUSTAFA DURDAĞ received the B.Sc., M.Sc., and Ph.D. degrees in geomatics engineering from Yıldız Technical University, İstanbul, Türkiye, in 2010, 2013, and 2019, respectively. He is currently an Associate Professor with Artvin Çoruh University, Artvin, Türkiye, and a Postdoctoral Researcher with the Chair of Space Geodesy, ETH Zürich, Switzerland. His research interests include geodetic reliability theory, outlier detection, deformation analysis, and GNSS interferometric reflectometry.



ÖMER KASAR received the B.E., M.Sc., and Ph.D. degrees in electronics and communication engineering from Süleyman Demirel University, in 2011, 2015, and 2019, respectively. His career trajectory includes serving as an Assistant Professor at the Department of Electrical and Electronics Engineering, Artvin Çoruh University, from 2019 to 2024. He has been an Associate Professor at the Electronics and Communication Engineering Department, Karadeniz Technical University, since 2024. His research interests have consistently focused on RF energy harvesting, broadband impedance matching, and microwave circuit design, with early work also mentioning frequency selective surfaces and RF systems for satellite communication.



CEMALI ALTUNTAS received the B.Sc., M.Sc., and Ph.D. degrees in geomatics engineering, with his doctoral research focusing on GNSS interferometric reflectometry (GNSS-IR). He was a Visiting Researcher at the National Oceanography Centre, Liverpool, U.K. He is currently a Research Assistant with Yıldız Technical University. His research interests include environmental monitoring applications, particularly sea-level estimation using GNSS-IR, as well as precise positioning techniques and advanced GNSS signal processing.



HAYRUNNISA UMUTLU is currently pursuing the bachelor's degree in electronics and communication engineering with Karadeniz Technical University. Her research interests include RF communications, GNSS technologies, and embedded systems.



SIMON WILLIAMS received the Ph.D. degree in geodetic geophysics from Durham University, U.K. He worked at the Scripps Institution of Oceanography before moving to the National Oceanography Centre. His research interests include the stochastic modeling of time series, sea level and vertical land motion, and the development of GNSS-IR.